

# SCIENTIFIC REPORTS



OPEN

## Ultrasmall Fe<sub>2</sub>O<sub>3</sub> nanoparticles/ MoS<sub>2</sub> nanosheets composite as high-performance anode material for lithium ion batteries

Bin Qu<sup>1,2</sup>, Yue Sun<sup>1</sup>, Lianlian Liu<sup>1</sup>, Chunyan Li<sup>1</sup>, Changjian Yu<sup>1</sup>, Xitian Zhang<sup>2</sup> & Yujin Chen<sup>1</sup>

Coupling ultrasmall Fe<sub>2</sub>O<sub>3</sub> particles (~4.0 nm) with the MoS<sub>2</sub> nanosheets is achieved by a facile method for high-performance anode material for Li-ion battery. MoS<sub>2</sub> nanosheets in the composite can serve as scaffolds, efficiently buffering the large volume change of Fe<sub>2</sub>O<sub>3</sub> during charge/discharge process, whereas the ultrasmall Fe<sub>2</sub>O<sub>3</sub> nanoparticles mainly provide the specific capacity. Due to bigger surface area and larger pore volume as well as strong coupling between Fe<sub>2</sub>O<sub>3</sub> particles and MoS<sub>2</sub> nanosheets, the composite exhibits superior electrochemical properties to MoS<sub>2</sub>, Fe<sub>2</sub>O<sub>3</sub> and the physical mixture Fe<sub>2</sub>O<sub>3</sub>+MoS<sub>2</sub>. Typically, after 140 cycles the reversible capacity of the composite does not decay, but increases from 829 mA h g<sup>-1</sup> to 864 mA h g<sup>-1</sup> at a high current density of 2 A g<sup>-1</sup>. Thus, the present facile strategy could open a way for development of cost-efficient anode material with high-performance for large-scale energy conversion and storage systems.

Owing to their high energy densities and environmental benignity, lithium ion batteries (LIBs) have been used as potential power sources for various electronic devices and equipments, ranging from a tiny music player to a massive sports car<sup>1,2</sup>. However, the commercial graphite anode of LIBs is difficult to satisfy the requirements of high power equipment of the modern society due to its low specific capacity (372 mA h g<sup>-1</sup>). Thus, alternative anode materials with good electrochemical performances are particularly desirable. 2H-MoS<sub>2</sub>, as a typical member of transition metal dichalcogenides, is composed of a layer of molybdenum atoms sandwiched between two layers of sulphur atoms. The spacing between neighboring layers is 0.615 nm, significantly larger than that of graphite (0.335 nm), and the weak van der Waals forces between the layers allows Li ions to diffuse without a significant increase in volume, leading to high-performance of MoS<sub>2</sub> as anode material than that of graphite<sup>3</sup>. The theoretical capacity of MoS<sub>2</sub> is as high as 670 mA h g<sup>-1</sup>, resulting from a conversion reaction of MoS<sub>2</sub>+4Li<sup>+</sup>+4e<sup>-</sup>→Mo+2Li<sub>2</sub>S<sup>4,5</sup>. Furthermore, MoS<sub>2</sub> surface exists many unsaturated sulfur dangling bonds, which will also be involved in the charge and discharge reactions<sup>6</sup>, and consequently the actual capacity of MoS<sub>2</sub> is often higher than the theoretical value<sup>7-9</sup>. Recently, in order to improve the reversible capacity of MoS<sub>2</sub> many strategies were developed to synthesize various MoS<sub>2</sub> nanostructures including exfoliated MoS<sub>2</sub><sup>10</sup> and hollow MoS<sub>2</sub> nanosheet assemblies, nanotubes<sup>11,12</sup>, nanoboxes<sup>13,14</sup>, MoS<sub>2</sub>@void@MoS<sub>2</sub><sup>15</sup>, and hollow nanospheres<sup>16,17</sup>. Unfortunately, due to the poor conductivity, the MoS<sub>2</sub> materials exhibited inferior cycling stability and rate performance, which impedes their practical application<sup>10</sup>. One efficient solution is to introduce carbon materials, such as graphene nanosheets<sup>18-29</sup>, carbon nanotubes<sup>30-32</sup>, carbon nanospheres<sup>33</sup>, carbon fiber cloth<sup>34,35</sup>, mesoporous carbon<sup>36</sup> to improve the electrical conductivity of the composite materials. However, due to the lower capacity of these carbon materials, the overall energy density of the composite material would be suppressed.

Because of its high theoretical capacity (1005 mA h g<sup>-1</sup>), low cost, abundance in nature, and environmental benignity Fe<sub>2</sub>O<sub>3</sub> is another promising anode material<sup>37,38</sup>. Especially when Fe<sub>2</sub>O<sub>3</sub> in ultrasmall size (5~10 nm) can exhibit high rate electrochemical performances<sup>37,38</sup>. Firstly, the ultrasmall size can greatly mitigate the volume expansion/contraction of Fe<sub>2</sub>O<sub>3</sub> particles during charge/discharge. Secondly, a high lithium ion flux can be

<sup>1</sup>Key Laboratory of In-Fiber Integrated Optics, Ministry of Education and College of Science, Harbin Engineering University, Harbin 150001, China. <sup>2</sup>Key Laboratory for Photonic and Electronic Bandgap Materials, Ministry of Education and School of Physics and Electronic Engineering, Harbin Normal University, Harbin 150025, China. Correspondence and requests for materials should be addressed to C.L. (email: chunyanli@hrbeu.edu.cn) or Y.C. (email: chenYujin@hrbeu.edu.cn)

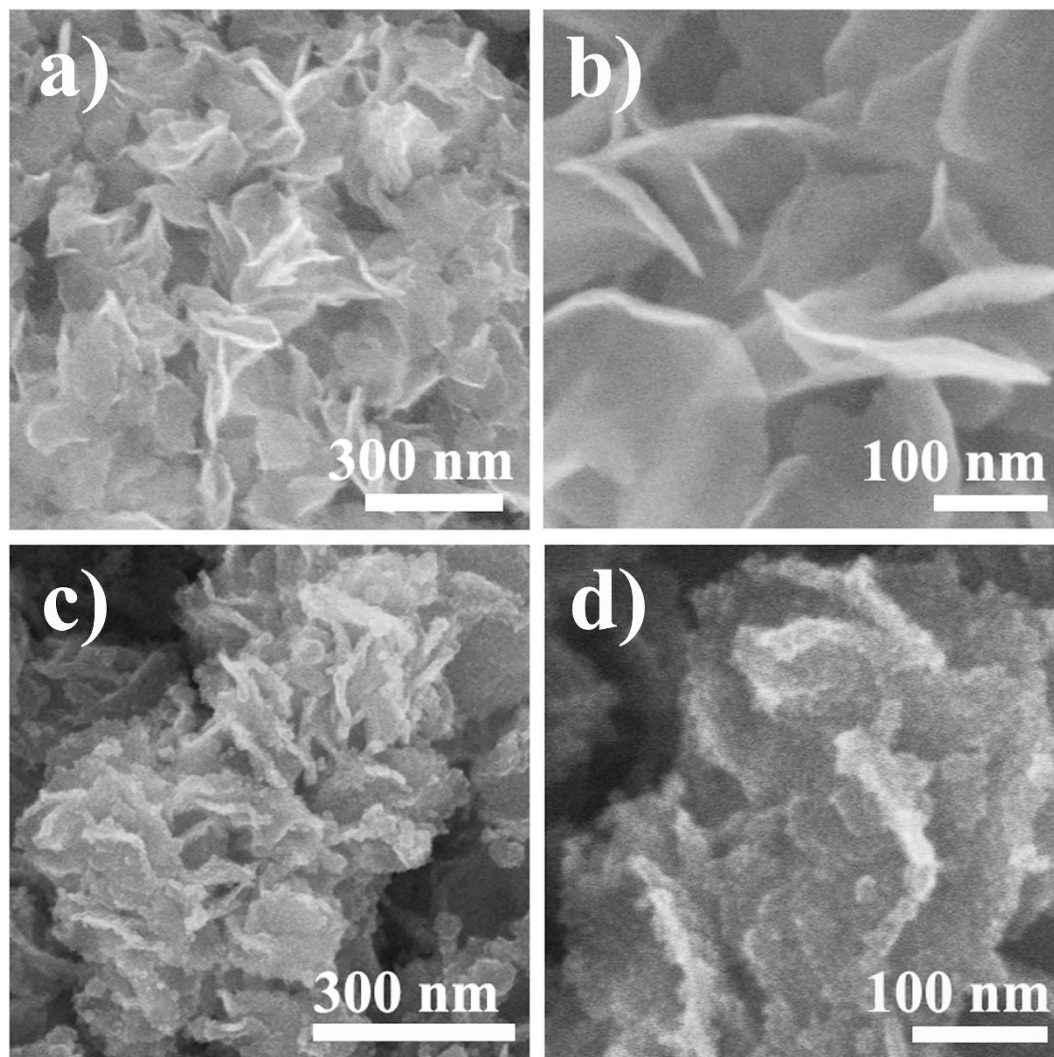


**Figure 1. Structural characterization of MoS<sub>2</sub> nanosheets and Fe<sub>2</sub>O<sub>3</sub>/MoS<sub>2</sub> composite.** (a,b) SEM of MoS<sub>2</sub> nanosheets, and (c,d) SEM of Fe<sub>2</sub>O<sub>3</sub>/MoS<sub>2</sub> composite.

achieved by the large surface area provided by the ultrasmall particles<sup>39</sup>. More importantly, due to the extremely short distance for lithium ions transportation within ultrasmall particles, the rate capability of lithium insertion/removal can be significantly enhanced<sup>40</sup>. However, the nanostructured Fe<sub>2</sub>O<sub>3</sub> exhibited a poor cycling stability due to structural damage during charging/discharging process<sup>37</sup>.

Herein, we report a facile method to grow ultrasmall Fe<sub>2</sub>O<sub>3</sub> nanoparticles on 2H-MoS<sub>2</sub> nanosheets, where MoS<sub>2</sub> nanosheets in the composite can serve as scaffolds, efficiently buffering the large volume changes of Fe<sub>2</sub>O<sub>3</sub> during charging/discharging process, whereas the ultrasmall Fe<sub>2</sub>O<sub>3</sub> nanoparticles mainly provide the specific capacity of the anode as well as the enhanced electrical conductivity. Furthermore, strong coupling between Fe<sub>2</sub>O<sub>3</sub> and MoS<sub>2</sub> nanosheets, elucidated by X-ray photoelectron spectrum measurements, facilitates a rapid charge transfer. In addition, MoS<sub>2</sub> nanosheets in the composite can also contribute to the total capacity of the anode. As a consequence, the composite prepared here exhibited superior electrochemical performance for anode material for Li-ion battery.

## Results

SEM images (Fig. 1a and b) show that the as-prepared MoS<sub>2</sub> exhibits sheet-like morphology with a thickness and a lateral length of about 10 and 400 nm, respectively, similar to that reported previously<sup>41</sup>. After Fe<sub>2</sub>O<sub>3</sub> coating, the MoS<sub>2</sub> exhibits a similar morphology and lateral length to that of the pristine MoS<sub>2</sub> nanosheets, but the surface becomes drastically rough (Fig. 1c), in sharp contrast to the smooth surface of the pristine MoS<sub>2</sub> nanosheets (Fig. 1b). From the high-magnification SEM image of the composite (Fig. 1d)), it can also be found that many ultrasmall particles are anchored on both sides of basal planes of MoS<sub>2</sub> nanosheets. Figure 2a shows a TEM image taken from the basal plane of MoS<sub>2</sub> nanosheets in the composite. It can be found that Fe<sub>2</sub>O<sub>3</sub> nanoparticles are uniformly and densely deposited on the surface of the MoS<sub>2</sub> nanosheets. The size distribution plot (Figure S1) indicates that the average size of Fe<sub>2</sub>O<sub>3</sub> nanoparticles is about 4.0 nm. Most lattice fringes of the Fe<sub>2</sub>O<sub>3</sub> nanoparticles in the high-resolution TEM (HRTEM) image (Fig. 2b) are not resolved well, revealing the weak degree of

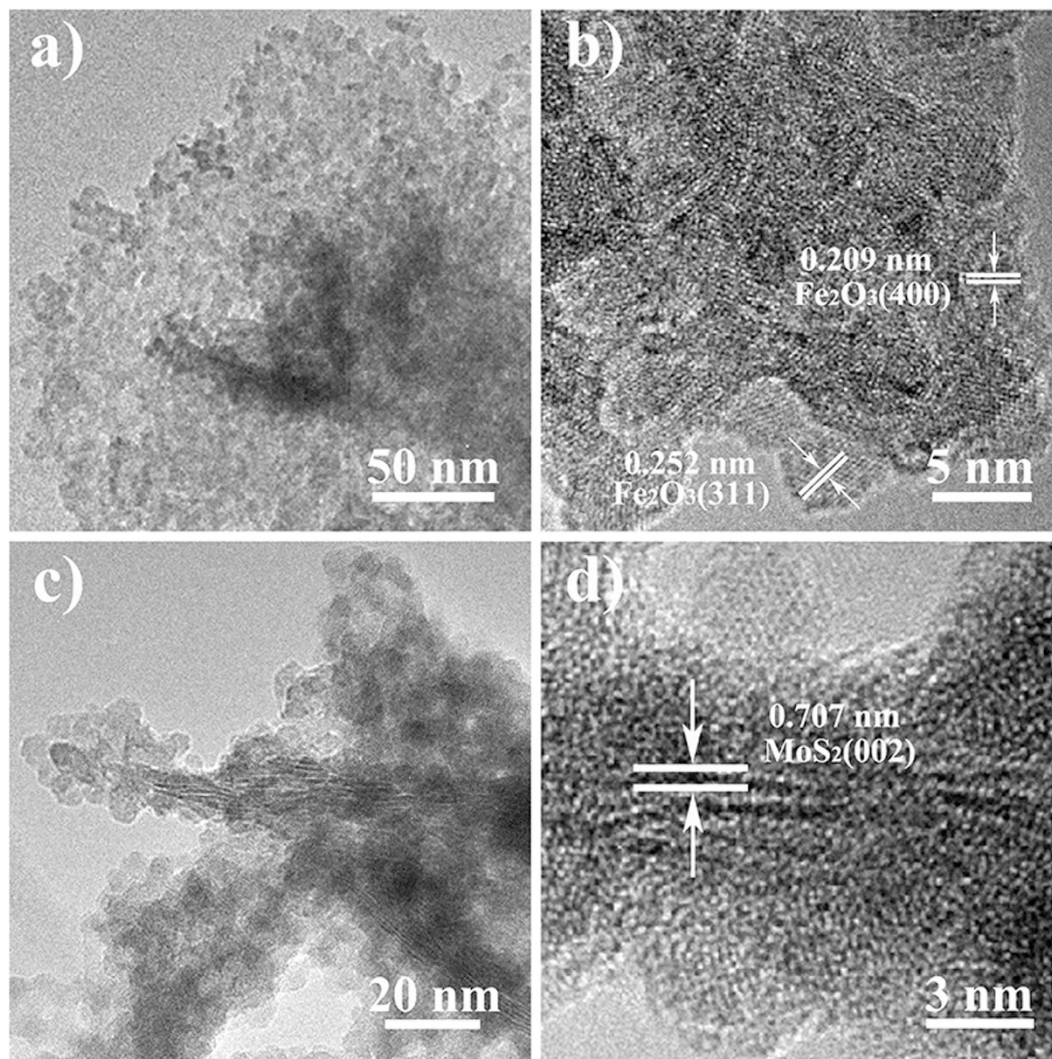


**Figure 2.** TEM image of  $\text{Fe}_2\text{O}_3/\text{MoS}_2$  composite. (a,b) TEM and HRTEM images taken from basal plane, and (c,d) cross-section TEM and HRTEM image of basal plane.

crystallizations of the  $\text{Fe}_2\text{O}_3$  nanoparticles. The labeled lattice spacing for  $\text{Fe}_2\text{O}_3$  nanoparticles in the HRTEM image is about 0.209 nm and 0.252 nm, which can be assigned to the (400) plane and (311) plane of  $\text{Fe}_2\text{O}_3$ , respectively. The fast Fourier transformation (FFT) technique confirms the crystal nature of  $\text{Fe}_2\text{O}_3$  on the  $\text{MoS}_2$  nanosheets (Figure S2). Cross-section TEM image (Fig. 2c) reveals that the ultrasmall  $\text{Fe}_2\text{O}_3$  nanoparticles mainly disperse on the basal planes of the  $\text{MoS}_2$  nanosheets, in which the lattice fringes corresponding to (002) plane can be clearly observed. HRTEM image (Fig. 2d) reveals that the interlayer distance of the (002) plane of the  $\text{MoS}_2$  nanosheets is about 0.707 nm, larger than the value (0.615 nm) of bulk  $\text{MoS}_2$ .

The crystal structures of the samples were examined using X-ray diffraction (XRD) measurement. Figure 3a shows the XRD pattern of the pristine  $\text{MoS}_2$  nanosheets, in which the peaks located at  $2\theta = 32.2^\circ$  corresponds to the (100) and (101) planes,  $2\theta = 38.3^\circ$  corresponds to the (103) plane and the peaks located at  $2\theta = 57.3^\circ$  corresponds to the (110) and (008) planes of 2H- $\text{MoS}_2$  (JCPDS No. 37-1492). Compared to 2H- $\text{MoS}_2$  bulk, these peaks slightly shift toward low-angle region, revealing the slightly enlarged lattice distances along the basal planes of 2H- $\text{MoS}_2$ . Similar to the previous report<sup>41</sup>, two additional peaks located at  $9.2^\circ$  and  $18.5^\circ$ , marked by “#”, are also observed at low-angle region. The corresponding  $d$ -spacings calculated according to the Bragg equation are 0.96 and 0.48 nm, respectively. The diploid relation between the  $d$ -spacings reveals that the  $\text{MoS}_2$  nanosheets possess a new lamellar structure with a larger interlayer spacing of 0.96 nm than that of 0.615 nm in bulk 2H- $\text{MoS}_2$ <sup>34,41,42</sup>. The enlarged interlayer spacing may be related to the synthesis conditions<sup>28,34,41,42</sup>. As previously reported<sup>41</sup>, when the temperature was lower than  $180^\circ\text{C}$ , the  $\text{MoS}_2$  nanosheets with enlarged interlayer spacing (0.95 nm) could be obtained in alkaline media; while the temperature was increased to  $220^\circ\text{C}$ , the interlayer distance of the nanosheets kept the same value as that in bulk  $\text{MoS}_2$ <sup>41</sup>. On the other hand, the enlarged interlayer spacing could be achieved in the media containing urea at  $220^\circ\text{C}$ ; however, when the pH in the media was decreased by replacing urea with ammonium fluoride, even at the same temperature the phenomenon did not occur<sup>42</sup>. Therefore, the alkalinity and the synthetic temperature seriously affect the interlayer distance of the  $\text{MoS}_2$  nanosheets. Under

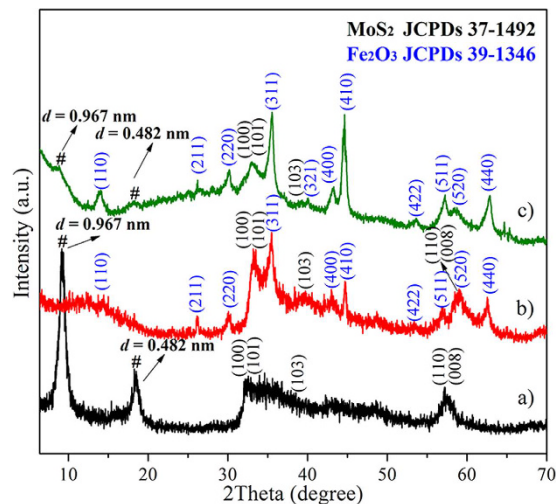


**Figure 3.** XRD patterns. (a) MoS<sub>2</sub> nanosheets, (b) Fe<sub>2</sub>O<sub>3</sub>/MoS<sub>2</sub> composite and (c) the physical mixture Fe<sub>2</sub>O<sub>3</sub>+MoS<sub>2</sub>.

the experimental conditions such as strong alkaline media and low temperature, oxygen species may incorporate more easily with MoS<sub>2</sub>, leading to the different lamellar structure with a enlarged interlayer spacing than that of 0.615 in bulk 2H-MoS<sub>2</sub><sup>34,41,42</sup>. However, the new lamellar structure is thermodynamically unstable. After annealing the MoS<sub>2</sub> nanosheets at 500 °C for 3 h under an Ar flow, XRD analysis was carried out. As shown in Figure S3, the diffraction peaks at 9.2° and 18.5° disappear, while all the resolved peaks can be assigned to thermodynamically stable 2H-MoS<sub>2</sub> (JCPDS No. 37–1492). After Fe<sub>2</sub>O<sub>3</sub> coating, the peak corresponding to the (002) plane is suppressed significantly, further suggesting that uniform and dense nanoparticles are deposited on the both sides of the basal plane of the MoS<sub>2</sub> nanosheets (Fig. 3b). In addition, the peaks from the Fe<sub>2</sub>O<sub>3</sub> and MoS<sub>2</sub> can also be identified in the XRD pattern. The diffraction peaks at  $2\theta = 33.4^\circ$  can be assigned to (100) and (101) planes,  $2\theta = 39.5^\circ$  can be assigned to (103) plane and  $2\theta = 58.5^\circ$  can be assigned to (110) and (008) planes of 2H-MoS<sub>2</sub>, respectively, whereas those at  $2\theta = 14.5^\circ, 26.1^\circ, 30.2^\circ, 35.5^\circ, 43.2^\circ, 44.6^\circ, 53.6^\circ, 57.1^\circ, 59.6^\circ$  and  $62.7^\circ$  can be indexed to (110), (211), (220), (311), (400), (410), (422), (511), (520) and (440) planes of Fe<sub>2</sub>O<sub>3</sub> (JCPDS no. 39–1346), respectively. Notably, the peak position of (110) plane in Fig. 3a is different from that in Fig. 3b. This is because the pristine MoS<sub>2</sub> nanosheets with the enlarged interlayer spacing are thermodynamically unstable phases, while the MoS<sub>2</sub> nanosheets in Fe<sub>2</sub>O<sub>3</sub>/MoS<sub>2</sub> composite, which were annealing at 500 °C for 3 h under an Ar flow, are thermodynamically stable. They had different lamellar structures, leading to significantly difference in XRD results (Fig. 3 and Figure S4). Compared to the XRD pattern of the annealed MoS<sub>2</sub> nanosheets with that of the Fe<sub>2</sub>O<sub>3</sub>/MoS<sub>2</sub> composite, the peak position of (110) plane is almost identical (Figure S5). The above results demonstrate that crystalline Fe<sub>2</sub>O<sub>3</sub> nanoparticles are successfully anchored on the surface of MoS<sub>2</sub> nanosheets. Figure 3c) shows the XRD pattern of the physical mixture Fe<sub>2</sub>O<sub>3</sub>+MoS<sub>2</sub>, in which the diffraction peaks from both Fe<sub>2</sub>O<sub>3</sub> and MoS<sub>2</sub> can be observed. Notably, the diffraction peak corresponding to expanded (002) plane of MoS<sub>2</sub> nanosheets is still visible, significantly different from that of the Fe<sub>2</sub>O<sub>3</sub>/MoS<sub>2</sub> composite.

X-ray photoelectron spectroscopy (XPS) analysis was carried out to determine surface chemical compositions and valence states of the Fe<sub>2</sub>O<sub>3</sub>/MoS<sub>2</sub> composite and the MoS<sub>2</sub> nanosheets. Figure 4a shows the high-resolution XPS spectra of Mo 3d core level for the two samples. Two peaks at 231.9 eV and 228.7 eV are observed in the Mo 3d spectrum of the MoS<sub>2</sub> nanosheets, corresponding to Mo<sup>4+</sup> species. After coating Fe<sub>2</sub>O<sub>3</sub>, the two peaks shift to high binding energy side by an approximately 0.3 eV. The shift of the binding energy indicates that electron transfer from MoS<sub>2</sub> to Fe<sub>2</sub>O<sub>3</sub> occurs. It can be concluded that the strong coupling between MoS<sub>2</sub> and Fe<sub>2</sub>O<sub>3</sub> is presented in the composite. However, such shift in the physical mixture MoS<sub>2</sub>+Fe<sub>2</sub>O<sub>3</sub> does not occur (Figure S6), revealing the advantage of our method for preparation of the Fe<sub>2</sub>O<sub>3</sub>/MoS<sub>2</sub> composite. In addition, two additional peaks at 235.6 eV and 232.5 eV are assigned to Mo<sup>6+</sup> species<sup>43–45</sup>, suggesting the surface oxidation of MoS<sub>2</sub> due to the electron transfer. In the XPS spectrum of S 2p core level for the pure MoS<sub>2</sub> nanosheets, the main doublet located at binding energies of 161.6 and 162.9 eV correspond to the S 2p<sub>3/2</sub> and S 2p<sub>1/2</sub>, respectively (Fig. 4b)<sup>41</sup>. There are no obvious shift of the binding energy of the two peaks for the Fe<sub>2</sub>O<sub>3</sub>/MoS<sub>2</sub> composite, implying that the Fe<sub>2</sub>O<sub>3</sub> coating has little effect on the valence states of the S species. In the Fe 2p core level spectrum for the Fe<sub>2</sub>O<sub>3</sub>/MoS<sub>2</sub> composite, the peaks at 711.3 eV, 719.2 eV and 724.8 eV represent the binding energies of Fe 2p<sub>3/2</sub>, shake-up satellite Fe 2p<sub>3/2</sub>, and Fe 2p<sub>1/2</sub> of Fe<sup>3+</sup> species, respectively (Fig. 4c)<sup>46,47</sup>. These values are consistent with the data of Fe<sub>2</sub>O<sub>3</sub> reported by the previous literatures<sup>48,49</sup>, confirming the existence of Fe<sub>2</sub>O<sub>3</sub> in the Fe<sub>2</sub>O<sub>3</sub>/MoS<sub>2</sub> composite. Compared to the XPS spectra of Fe<sub>2</sub>O<sub>3</sub> in the physical mixture MoS<sub>2</sub>+Fe<sub>2</sub>O<sub>3</sub>, the peaks for Fe 2p<sub>1/2</sub> and Fe 2p<sub>3/2</sub> shift to low binding energy side, further confirming the coupling effect between Fe<sub>2</sub>O<sub>3</sub> and MoS<sub>2</sub> in the Fe<sub>2</sub>O<sub>3</sub>/MoS<sub>2</sub> composite. The peaks 529.9 and 530.0 eV in the high-resolution XPS spectrum of O 1s core level for the Fe<sub>2</sub>O<sub>3</sub>/MoS<sub>2</sub> composite can be assigned to oxygen in the lattice (Fe–O)<sup>50,51</sup> and oxygen in the lattice (Mo–O)<sup>41</sup>, respectively (Fig. 4d). Besides, the peak at 531.5 eV is associated to the hydroxyl oxygen.

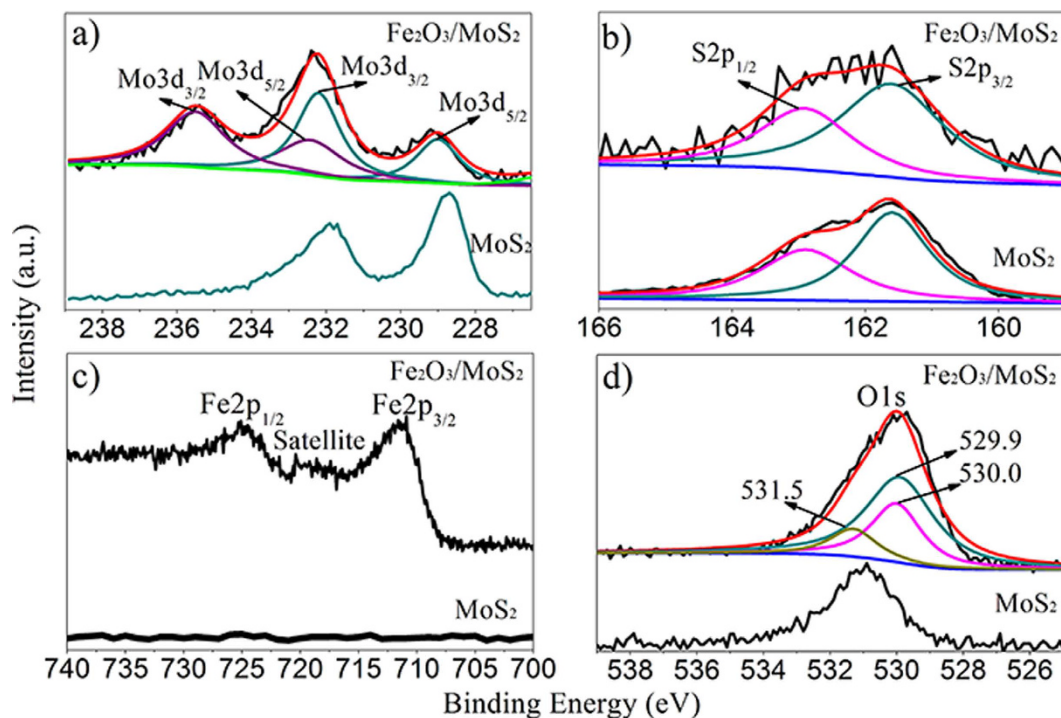


**Figure 4.** XPS spectra of  $\text{Fe}_2\text{O}_3/\text{MoS}_2$  composite and  $\text{MoS}_2$  nanosheets. (a) Mo 3d XPS spectrum, (b) S 2p XPS spectra, (c) Fe 2p XPS spectrum, and (d) O 1s XPS spectrum.

Cyclic voltammogram (CV) tests for coin cells of the pristine  $\text{MoS}_2$  nanosheets were recorded at ambient temperature in the voltage range of 0.01–3 V at a scan rate of  $1 \text{ mV s}^{-1}$  for the initial five cycles, as shown in Fig. 5a. The peak of 0.87 V in the first cathodic scanning is ascribed to the intercalation of lithium ion on different defect sites in  $\text{MoS}_2$  to form  $\text{Li}_x\text{MoS}_2$ . In the following cathodic scanning, two new reduction peaks at approximately 1.65 V and 1.15 V are observed, which are due to the conversion of S to  $\text{Li}_2\text{S}$  and the association of Li with Mo respectively<sup>52,53</sup>. During the anodic scans, two peaks at 1.92 and 2.42 V are clearly observed and maintain for the subsequent sweeps, which are related to the conversion reaction of Mo and  $\text{Li}_2\text{S}$  to  $\text{MoS}_2$  phase<sup>54,55</sup>. As for the pure  $\text{Fe}_2\text{O}_3$  in Fig. 5b, the reduction peaks at 0.36 V is observed in the first cycle, and its position shifts to 0.57 V at the following scanning, which is attributed to the reduction of Fe(III) to Fe(0). In the anodic scans, the oxidation peak at 1.95 V is the oxidation of Fe to  $\text{Fe}_2\text{O}_3$ . As for the  $\text{Fe}_2\text{O}_3/\text{MoS}_2$  composite, three reduction peaks at 0.36 V, 0.87 V and 1.20 V are observed in the first cycle (Fig. 5c). The reduction peaks locate at 0.36 V and 0.87 V during the first anodic scan can match anodic scan peaks of pure  $\text{Fe}_2\text{O}_3$  and pure  $\text{MoS}_2$ , respectively. The peak located at 1.20 V shows a same start shoulder at  $\sim 1.05$  V with pure  $\text{MoS}_2$ , which suggest the same lithiation process of  $\text{MoS}_2$ <sup>8</sup>. At the following scanning, however, these peaks shift to 0.65 V, 1.15 V and 1.75 V respectively. The peak at 1.15 V is related to the conversion of  $\text{MoS}_2$  to Mo and  $\text{Li}_2\text{S}$ , while two other peaks at 1.75 and 0.65 V are attributed to the formation of  $\text{Li}_x\text{Fe}_2\text{O}_3$  due to the lithiation of  $\text{Fe}_2\text{O}_3$  and the reduction of Fe(III) to Fe(0), respectively<sup>56–60</sup>. In the anodic scans, the oxidation peaks at 1.82 V and 2.40 V stand for oxidation of Mo to  $\text{MoS}_2$  and Fe to  $\text{Fe}_2\text{O}_3$ , respectively. The CV results demonstrate that both  $\text{Fe}_2\text{O}_3$  and  $\text{MoS}_2$  in the composite contribute to the capacity of the composite. As for the physical mixture  $\text{Fe}_2\text{O}_3+\text{MoS}_2$  (Fig. 5d), three reduction peaks at 0.43 V, 1.04 V and 1.30 V are found in the first cycle, and then their positions shift to 0.71 V, 1.16 V and 1.81 V after the following scanning, respectively, which are close to the positions of the corresponding peaks for  $\text{Fe}_2\text{O}_3/\text{MoS}_2$  composite (Fig. 5c). In the anodic scans, the oxidation peaks are also in accordance with  $\text{Fe}_2\text{O}_3/\text{MoS}_2$  composite. The observations suggest that similar electrochemical reactions occur for  $\text{Fe}_2\text{O}_3+\text{MoS}_2$  and  $\text{Fe}_2\text{O}_3/\text{MoS}_2$  composites during charging/discharging process. However, the physical mixture  $\text{Fe}_2\text{O}_3+\text{MoS}_2$  has larger irreversible capacity than the  $\text{Fe}_2\text{O}_3/\text{MoS}_2$  composite, as shown in Fig. 5c and d, suggesting advantage of coupling ultrasmall  $\text{Fe}_2\text{O}_3$  nanoparticles with  $\text{MoS}_2$  nanosheets. Figure 5e–h show the voltage–capacity curves of pristine  $\text{MoS}_2$  nanosheets, pure  $\text{Fe}_2\text{O}_3$ ,  $\text{Fe}_2\text{O}_3/\text{MoS}_2$  composite and physical mixture  $\text{Fe}_2\text{O}_3+\text{MoS}_2$  at a current density of  $100 \text{ mA g}^{-1}$ . The initial discharging/charging capacities of the  $\text{Fe}_2\text{O}_3/\text{MoS}_2$  composite are  $1366/1207 \text{ mA h g}^{-1}$ , greatly larger than that of pure  $\text{MoS}_2$  nanosheets ( $854/754 \text{ mA h g}^{-1}$ ), pure  $\text{Fe}_2\text{O}_3$  ( $1218/879 \text{ mA h g}^{-1}$ ) and the physical mixture  $\text{Fe}_2\text{O}_3+\text{MoS}_2$  ( $1056/815 \text{ mA h g}^{-1}$ ). Furthermore, the  $\text{Fe}_2\text{O}_3/\text{MoS}_2$  composite has a Coulombic efficiency of 88.4% at the first cycle, much higher than that of the physical mixture  $\text{Fe}_2\text{O}_3+\text{MoS}_2$  (77.2%), consistent with the CV results. The energy efficiency (discharge energy/charge energy) of the  $\text{Fe}_2\text{O}_3/\text{MoS}_2$  composite are 43%–58% (Figure S7). The larger specific capacity and higher Coulombic efficiency of the  $\text{Fe}_2\text{O}_3/\text{MoS}_2$  composite indicate that coupling ultrasmall  $\text{Fe}_2\text{O}_3$  particles with  $\text{MoS}_2$  nanosheets is an efficient strategy to improve the electrochemical performance of the  $\text{MoS}_2$  nanosheets.

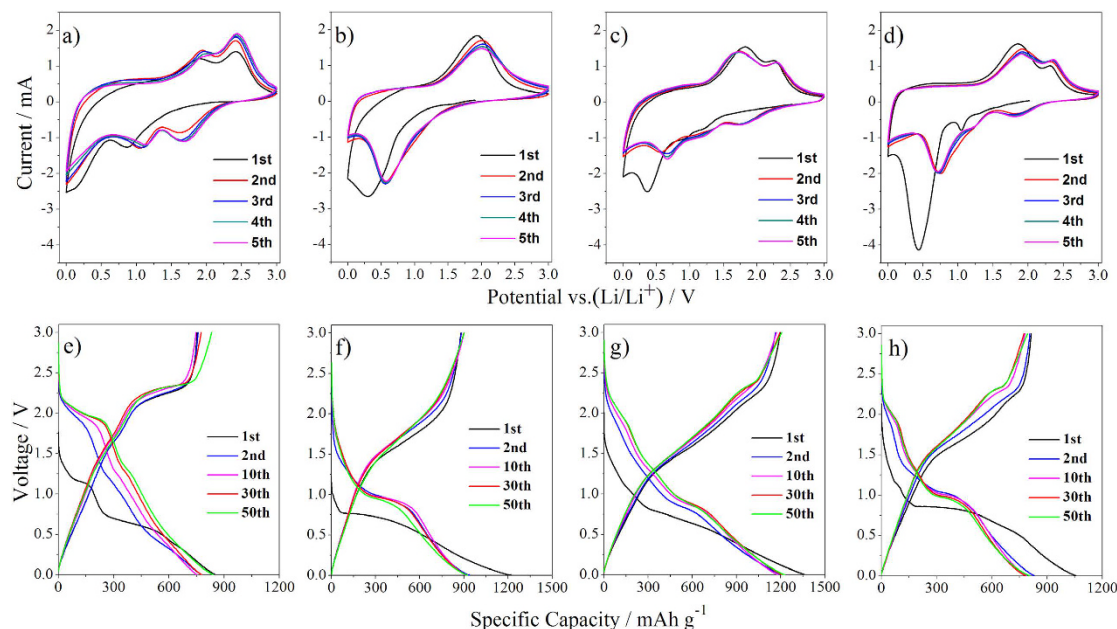


**Figure 5.** CV curves of (a) MoS<sub>2</sub> nanosheets, (b) Fe<sub>2</sub>O<sub>3</sub>, (c) Fe<sub>2</sub>O<sub>3</sub>/MoS<sub>2</sub> composite and (d) the physical mixture Fe<sub>2</sub>O<sub>3</sub>+MoS<sub>2</sub>, and charging–discharging curves of (e) MoS<sub>2</sub> nanosheets, (f) Fe<sub>2</sub>O<sub>3</sub>, (g) Fe<sub>2</sub>O<sub>3</sub>/MoS<sub>2</sub> composite and (h) the physical mixture Fe<sub>2</sub>O<sub>3</sub>+MoS<sub>2</sub>.

To confirm the superiority of the Fe<sub>2</sub>O<sub>3</sub>/MoS<sub>2</sub> composite as an anode material over the pristine MoS<sub>2</sub> nanosheets and the physical mixture Fe<sub>2</sub>O<sub>3</sub>+MoS<sub>2</sub> in the lithium storage performance, we compared their cycling behaviors at different current densities (Fig. 6). Clearly, MoS<sub>2</sub> nanosheets deliver an initial capacity of 854 mAh g<sup>-1</sup> at a current density of 100 mA g<sup>-1</sup> (Fig. 6a), higher than its theoretical value due to its ultra-thin nanosheets for lithium storage. However, obvious capacity decay is witnessed when cycled at a high current density (Fig. 6a). For example, the capacity decreases from 638 mA h g<sup>-1</sup> to 449 mA h g<sup>-1</sup> at 1 A g<sup>-1</sup> only after 40 cycles. This phenomenon is probably due to the exfoliation of the ultra-thin MoS<sub>2</sub> nanosheets during discharging/charging process. Similarly, the pure Fe<sub>2</sub>O<sub>3</sub> delivers an initial discharge capacity of 1219 mAh g<sup>-1</sup> at a current density of 100 mA g<sup>-1</sup>, and the capacity decreases from 533 mAh g<sup>-1</sup> to 287 mAh g<sup>-1</sup> at 1 A g<sup>-1</sup> only after 55 cycles (Fig. 6b). As the MoS<sub>2</sub> nanosheets are mixed with Fe<sub>2</sub>O<sub>3</sub> mechanically, slightly better cycling stability at the current densities of 100 mA g<sup>-1</sup> and 1 A g<sup>-1</sup> than the pristine MoS<sub>2</sub> nanosheets can be achieved, as shown in Fig. 6c. However, the physical mixture still shows poor cycling stability at a high current density. For example, the discharge capacity of the physical mixture decreases from 698 mA h g<sup>-1</sup> to 545 mA h g<sup>-1</sup> after 80 cycles at a high current density of 1 A g<sup>-1</sup> (Fig. 6c). In contrast, the Fe<sub>2</sub>O<sub>3</sub>/MoS<sub>2</sub> composite exhibits drastically enhanced rate capability (Fig. 6d,e and Figure S8). Furthermore, the Fe<sub>2</sub>O<sub>3</sub>/MoS<sub>2</sub> composite shows an excellent cycling durability at different current densities. For example, the Fe<sub>2</sub>O<sub>3</sub>/MoS<sub>2</sub> composite delivers an initial discharge capacity of 1366 mAh g<sup>-1</sup> at current densities of 100 mA g<sup>-1</sup>. The capacity does not decay after 150 cycles, but gradually increases to 1350 mA h g<sup>-1</sup> with a high Coulombic efficiency of >98.7% (Fig. 6d). Surprisingly, even at high current densities of 1 and 2 A g<sup>-1</sup>, the composite also exhibits excellent cycling stability (Fig. 6e). The capacity of the Fe<sub>2</sub>O<sub>3</sub>/MoS<sub>2</sub> composite increases from 908 mA h g<sup>-1</sup> to 1011 mA h g<sup>-1</sup> at 1 A g<sup>-1</sup>, and from 829 mA h g<sup>-1</sup> to 864 mA h g<sup>-1</sup> at 2 A g<sup>-1</sup> after 140 cycles (Fig. 6e). The cycling performance is inferior to that of MoS<sub>2</sub>/graphene composite with the capacity of 907 mA h g<sup>-1</sup> after 400 cycles<sup>29</sup>, however, comparable or superior to most other Fe<sub>2</sub>O<sub>3</sub> and MoS<sub>2</sub> or their composites, which is summarized in Table S1<sup>8,13,21,37,61–71</sup>. For example, the capacity of Fe<sub>2</sub>O<sub>3</sub> nanoparticles was only about 300 mAh g<sup>-1</sup> at ca. 100 mA g<sup>-1</sup> after 100 cycles<sup>37</sup>; the capacity of CNTs–MoS<sub>2</sub> was 737 mAh g<sup>-1</sup> at 100 mA g<sup>-1</sup> after 30 cycles<sup>69</sup>. Furthermore, when the current density is increased to 5 A g<sup>-1</sup>, the composite shows a relatively bad cycling durability, but still delivers a capacity of 481 mAh g<sup>-1</sup> after 140 cycles. To reveal the charge/discharge stability of anode, the SEM and elemental mapping analyses of Fe<sub>2</sub>O<sub>3</sub>/MoS<sub>2</sub> composite after 100 cycles were carried out. After the cycling, the ultrasmall Fe<sub>2</sub>O<sub>3</sub> nanoparticles are still resolved in the basal planes of the MoS<sub>2</sub> nanosheets, as shown in Figure S9. Elemental mapping images (Figure S10) reveal that Fe and Mo elements are uniformly distributed in the composite. These results above demonstrate that the Fe<sub>2</sub>O<sub>3</sub>/MoS<sub>2</sub> composite exhibit significantly enhanced capacity, rated capability and cycling stability compared to the pristine MoS<sub>2</sub> nanosheets, the pure Fe<sub>2</sub>O<sub>3</sub> and the physical mixture Fe<sub>2</sub>O<sub>3</sub>+MoS<sub>2</sub>. Notably, the electrochemical performance of Fe<sub>2</sub>O<sub>3</sub>/MoS<sub>2</sub> composite was measured at room temperature. It is well known that the electrochemical performance of the anode material for LIBs is suppressed significantly at the ambient temperature lower than 0 °C. However, as previously reported, the specific capacity of MoS<sub>2</sub>/G electrode at –20 °C still remained ca. 700 mAh g<sup>-1</sup> at 100 mA g<sup>-1</sup><sup>129</sup>. This result indicates that MoS<sub>2</sub>-based anode material may be used at low-temperature environment. The electrochemical performance of our Fe<sub>2</sub>O<sub>3</sub>/MoS<sub>2</sub> composite at such low-temperature environment is studied under way.

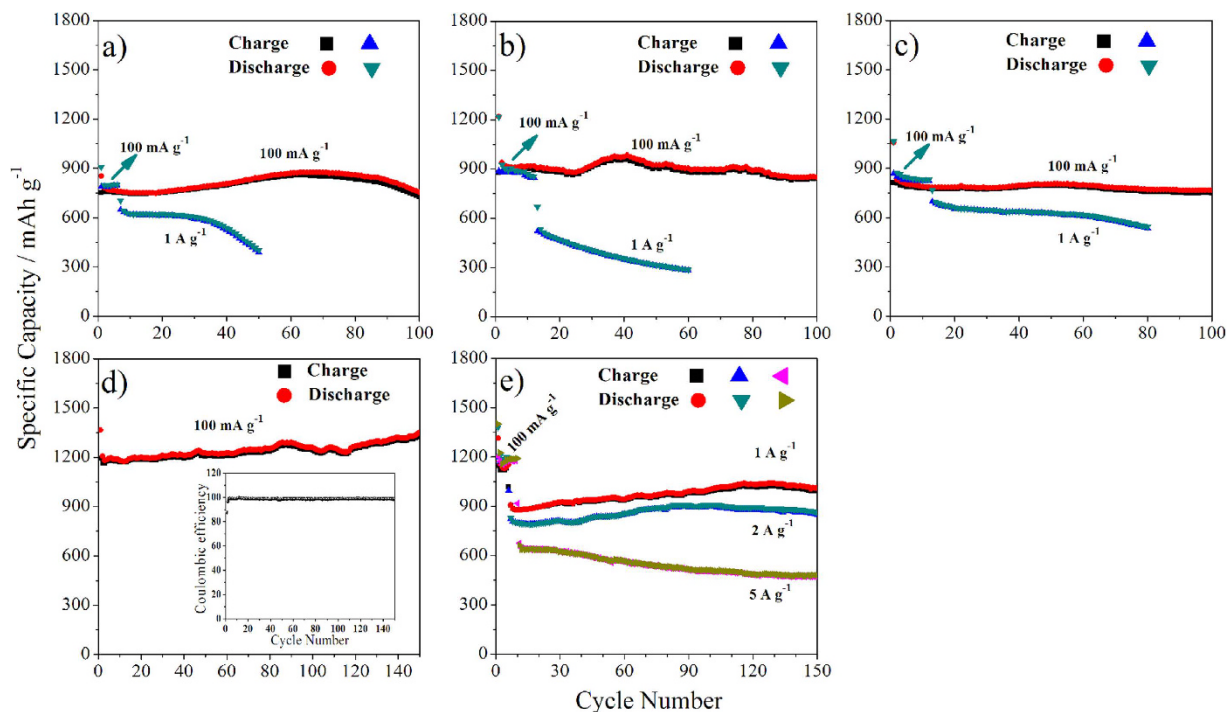


**Figure 6.** Cycling stability of samples at different current densities. (a) MoS<sub>2</sub> nanosheets at 100 and 1000 mA g<sup>-1</sup>, (b) Fe<sub>2</sub>O<sub>3</sub> at 100 and 1000 mA g<sup>-1</sup>, (c) the physical mixture Fe<sub>2</sub>O<sub>3</sub>+MoS<sub>2</sub> at 100 and 1000 mA g<sup>-1</sup>, (d) Fe<sub>2</sub>O<sub>3</sub>/MoS<sub>2</sub> composite at 100 mA g<sup>-1</sup>, the inset showing the corresponding Coulombic efficiency and (e) Fe<sub>2</sub>O<sub>3</sub>/MoS<sub>2</sub> composite at 1000 mA g<sup>-1</sup>, 2000 mA g<sup>-1</sup> and 5000 mA g<sup>-1</sup> (initial 6 cycles at 100 mA g<sup>-1</sup>).

## Discussion

The excellent electrochemical properties of the Fe<sub>2</sub>O<sub>3</sub>/MoS<sub>2</sub> composite, as evidenced by a remarkably increased reversible capacity, improved rate capability, and robust long-term stability even at a high current density, indicates that the Fe<sub>2</sub>O<sub>3</sub>/MoS<sub>2</sub> composite is favorable for superior anode materials for Li-ion battery. The following factors can be attributed to the improved electrochemical properties of the Fe<sub>2</sub>O<sub>3</sub>/MoS<sub>2</sub> composite. First, unlike some designed composites<sup>21,61,63,68,69,71</sup>, both Fe<sub>2</sub>O<sub>3</sub> and MoS<sub>2</sub> in our composite can contribute to the total capacity of the anode, elucidated by CV measurements (Fig. 5c). The high reversible capacity of the Fe<sub>2</sub>O<sub>3</sub>/MoS<sub>2</sub> composite may also be related to its unique heteronanostructure character. As we know, during the first discharge process, Fe<sub>2</sub>O<sub>3</sub> reacts with Li<sup>+</sup>, and then Fe and Li<sub>2</sub>O will gradually produce (Equation 1)<sup>72</sup>; however, only partial Li<sub>2</sub>O can reversibly converse to Li<sup>+</sup> during the subsequent charging process, leading to a high irreversible capacity of Fe<sub>2</sub>O<sub>3</sub>-based anodes. On the other hand, during the first discharging process of MoS<sub>2</sub>, amorphous Mo metal clusters will form (Equation 2) and disperse on the surface of MoS<sub>2</sub>. The Mo metal clusters have highly electrochemical activity<sup>73,74</sup>. Considering the unique heteronanostructure of the Fe<sub>2</sub>O<sub>3</sub>/MoS<sub>2</sub> composite, the Mo metal clusters on the MoS<sub>2</sub> surface can efficiently contact with Li<sub>2</sub>O and make the irreversible Li<sub>2</sub>O converse to Li<sup>+</sup>, as shown in Fig. 7a. As a result, the Fe<sub>2</sub>O<sub>3</sub>/MoS<sub>2</sub> composite shows a low irreversible capacity and a high Coulombic efficiency of 88.4% at the first cycle. As for the physical mixture Fe<sub>2</sub>O<sub>3</sub>+MoS<sub>2</sub>, since the efficient contact between Mo and Li<sub>2</sub>O is more difficultly available, the conversion of Li<sub>2</sub>O to Li<sup>+</sup> will be greatly suppressed (Fig. 7b). Consequently, the physical mixture Fe<sub>2</sub>O<sub>3</sub>+MoS<sub>2</sub> shows a high irreversible capacity and a low Coulombic efficiency at the first cycle (Fig. 5d and h).



Second, the average Fe<sub>2</sub>O<sub>3</sub> size is approximately 4.0 nm, which can shorten the Li ion transfer length and then facilitate the improvement of the rate capability. Additionally, nitrogen adsorption–desorption isotherms show that Brunauer–Emmett–Teller (BET) surface areas and cumulative volume of pores were 12.5 m<sup>2</sup> g<sup>-1</sup> and 0.06 cm<sup>3</sup> g<sup>-1</sup> for the pristine nanosheets, around two times lower than those of the composite (23.1 m<sup>2</sup> g<sup>-1</sup> and 0.12 cm<sup>3</sup> g<sup>-1</sup>), as shown in Figure S11 and Figure S12. The bigger BET surface area and larger pore volume not only allow for fast Li-ion diffusion, but also buffer the volume changes accompanying the Li charging and discharging processes<sup>28</sup>. Third, the strong coupled interfaces boost a rapid interfacial charge transfer, leading to excellent rate capability of the Fe<sub>2</sub>O<sub>3</sub>/MoS<sub>2</sub> composite, as evidenced by electrochemical impedance measurements. Nyquist plots (Fig. 8) shows that the Fe<sub>2</sub>O<sub>3</sub>/MoS<sub>2</sub> composite has a charge transfer resistance ( $R_{ct}$ ) of 39.9 Ω, greatly smaller than that of the physical mixture Fe<sub>2</sub>O<sub>3</sub>+MoS<sub>2</sub> (238.9 Ω), the pure Fe<sub>2</sub>O<sub>3</sub> (136.0 Ω) and the

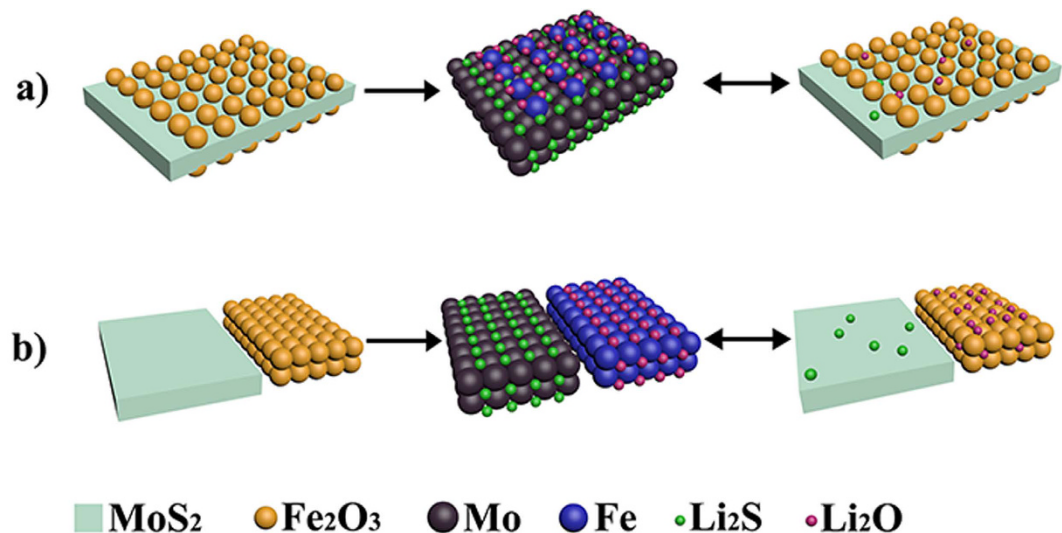


**Figure 7.** (a) Schematic illustration of the irreversible  $\text{Li}_2\text{O}$  convert to  $\text{Li}^+$  for the  $\text{Fe}_2\text{O}_3/\text{MoS}_2$  composite. Due to high electrochemical activity of Mo metal clusters and efficient contact between Mo metal clusters and the irreversible  $\text{Li}_2\text{O}$ , the irreversible  $\text{Li}_2\text{O}$  can convert to  $\text{Li}^+$  after the charging process, and (b) Schematic illustration of the irreversible  $\text{Li}_2\text{O}$  convert to  $\text{Li}^+$  for the physical mixture  $\text{Fe}_2\text{O}_3+\text{MoS}_2$ . The conversion of the irreversible  $\text{Li}_2\text{O}$  to  $\text{Li}^+$  will be greatly suppressed because the efficient contact between Mo and  $\text{Li}_2\text{O}$  is more difficultly available.

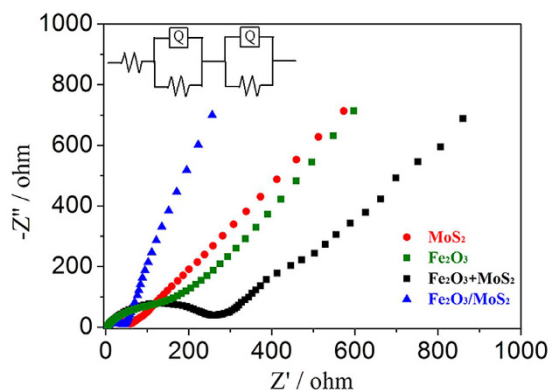


**Figure 8.** Nyquist plots for samples from 100 kHz to 0.01 Hz.

pristine  $\text{MoS}_2$  nanosheets ( $51.3 \Omega$ ), at high frequency 100000 Hz, Low frequency 0.01 Hz and amplitude 0.005 V. The strong coupling between  $\text{MoS}_2$  and  $\text{Fe}_2\text{O}_3$  implies that small  $\text{Fe}_2\text{O}_3$  nanoparticles are tightly anchored on the  $\text{MoS}_2$  scaffolds, facilitating long-term stability of the  $\text{Fe}_2\text{O}_3/\text{MoS}_2$  composite even at a high current density. Taken together, the synergistic effect of two excellent anode materials and the unique structural features of the composite make it an attractive candidate for anode material for Li-ion battery.

In summary, a facile and cost-effective strategy was developed to anchor ultras small  $\text{Fe}_2\text{O}_3$  nanoparticles on the surface of  $\text{MoS}_2$  nanosheets. Due to the synergistic effect of two excellent anode materials and the unique structural feature, the  $\text{Fe}_2\text{O}_3/\text{MoS}_2$  composite exhibits excellent electrochemical properties, including a remarkably increased reversible capacity, improved rate capability, and long-term stability even at a high current density. After 140 cycles the reversible capacity of the composite does not decay, but increases from  $829 \text{ mA h g}^{-1}$  to  $864 \text{ mA h g}^{-1}$  at a high current density of  $2 \text{ A g}^{-1}$ , outperforming other  $\text{MoS}_2$ - and iron oxide-based anode materials previously reported. Thus, the facile strategy may open a way for development of cost-efficient anode material with high-performance for large-scale energy conversion and storage systems.

## Methods

**Synthesis of samples.**  $\text{MoS}_2$  nanosheets were first synthesized by a solution-based method<sup>40</sup>. Simply,  $(\text{NH}_4)_6\text{Mo}_7\text{O}_{24}\cdot 4\text{H}_2\text{O}$  (1 mmol) and thiourea (30 mmol) were dissolved in distilled water (35 mL) under vigorous stirring to form a homogeneous solution. After being stirred for 30 min, the solution was transferred into a 50 mL Teflon-lined stainless steel autoclave and maintained at  $180^\circ\text{C}$  for 24 h. The obtained products were collected by centrifugation, washed with distilled water and ethanol, and dried at  $40^\circ\text{C}$  under vacuum. The obtained  $\text{MoS}_2$

nanosheets (30 mg) was dispersed in ethyl alcohol (75 mL) and then iron acetylacetonate (0.5 mmol), distilled water (1.8 mL) and ammonia (2 mL) were added. After sonication for 15 min at room temperature the mixture was heated at 80 °C for 10 h in a water bath. The precipitates were separated by centrifugation, washed with distilled water and ethanol, and dried at 40 °C for 24 h under vacuum. The growth of ultra-small Fe<sub>2</sub>O<sub>3</sub> nanoparticles on the MoS<sub>2</sub> nanosheets was achieved after the dried powder was thermally treated at 500 °C for 3 h under an Ar flow. For convenience, the obtained sample denoted as Fe<sub>2</sub>O<sub>3</sub>/MoS<sub>2</sub> composite. As shown in Figure S13, the Fe and Mo atom ratio was 2:1. The Fe<sub>2</sub>O<sub>3</sub> was prepared by heating graphene-hollow iron oxide at 500 °C for 1.5 h under air atmosphere<sup>72</sup>, and then was thermally treated at 350 °C for 1 h under an Ar/H<sub>2</sub> flow. The physical mixture Fe<sub>2</sub>O<sub>3</sub> and MoS<sub>2</sub> (denoted as Fe<sub>2</sub>O<sub>3</sub>+MoS<sub>2</sub>) as reference sample was prepared by grinding the MoS<sub>2</sub> nanosheets and commercial Fe<sub>2</sub>O<sub>3</sub> powder according to Fe and Mo atomic ratio.

**Structure characterizations.** The morphology and size of the samples were characterized by scanning electron microscope (SEM, Hitachi SU 70) (Condition = Vacc = 15KV, Mag = x60.0k- x250k, Working Distance = 15800 um, Emission Current = 28000 nA) and a FEI Tecnai-F20 transmission electron microscope (TEM) equipped with a Gatan imaging filter (GIF), operated at an accelerating voltage of 200 kV, combined with HRTEM and EDX measurements. The crystal structure of the sample was determined by X-ray diffraction (XRD) [D/max 2550 V, Cu K $\alpha$  radiation] in the 2 $\theta$  range of 5–70°. (X-Ray 40 kV/100 mA, DivSlit 1 deg., RecSlit open, DivH.L.Slit 10mm, SctSlit 8.0mm, Step 0.02). X-ray photoelectron spectra (XPS) were carried out by using a spectrometer with Mg K $\alpha$  radiation (PHI 5700 ESCA System). The binding energy was calibrated with the C 1s position of contaminant carbon in the vacuum chamber of the XPS instrument (284.6 eV). The pore diameter distribution and surface area were tested by nitrogen adsorption/desorption analysis (TRISTAR II3020).

**Electrochemical measurements.** The electrochemical tests were performed at ambient temperature using two-electrode coin cells (CR 2016) with lithium foils serving as the counter electrode. The active material was mixed with a conductive acetylene black, and a commercial polymer binder (LA133) at a weight ratio of 70:15:15. The mixture was painted onto a Cu foil and dried in air, then cut into 14 mm diameters of round piece. Finally the electrode pieces were dried in vacuum at 60 °C for 12 h to adequately evaporate the residual moisture. The average thickness and mass loading of the electrode were  $\sim$ 3.5  $\mu$ m (Figure S14) and  $1.5 \pm 0.2$  mg, respectively. The electrolyte was made of LiPF<sub>6</sub> (1 M) in a mixture of ethylene carbonate (EC) and dimethyl carbonate (DMC) with the volume ratio 1:1. The 2016 coin-type cells were assembled in an Ar filled glove box, and pure Li foils were used as the counter electrodes. The charge–discharge cycles were carried out on a battery measurement system (LAND-BT2013A) at various current densities of 100–5000 mA g<sup>-1</sup> in the cutoff voltage range of 3 to 0 V versus Li/Li<sup>+</sup> at room temperature ( $\sim$ 20 °C). Cyclic voltammetry measurements were carried out on a CHI660D electrochemical workstation over the potential range of 3.0 to 0.01 V at a scan rate of 1 mV s<sup>-1</sup>.

## References

- Armand, M. & Tarascon, J. M. Building better batteries. *Nature* **451**, 652–657 (2008).
- Tarascon, J. M. & Armand, M. Issues and challenges facing rechargeable lithium batteries. *Nature* **414**, 359–367 (2001).
- Wang, L. F., Xu, Z., Wang, W. L. & Bai, X. D. Atomic mechanism of dynamic electrochemical lithiation processes of MoS<sub>2</sub> nanosheets. *J. Am. Chem. Soc.* **136**, 6693–6697 (2014).
- Wang, Q. & Li, J. H. Facilitated lithium atorage in MoS<sub>2</sub> overlayers supported on coaxial carbon nanotubes. *J. Phys. Chem. C* **111**, 1675–1682 (2007).
- Yu, X. Y., Yu, L. & Lou, X. W. Metal sulfide hollow nanostructures for electrochemical energy storage. *Adv. Energy Mater.* **6**, 1501333 (2016).
- Liu, H. *et al.* Highly ordered mesoporous MoS<sub>2</sub> with expanded spacing of the (002) crystal plane for ultrafast lithium ion storage. *Adv. Energy Mater.* **2**, 970–975 (2012).
- Sen, U. K. & Mitra, S. High-rate and high-energy-density lithium-ion battery anode containing 2D MoS<sub>2</sub> nanowall and cellulose binder. *ACS Appl. Mater. Interfaces* **5**, 1240–1247 (2013).
- Sun, P. L. *et al.* Synthesis of hierarchical MoS<sub>2</sub> and its electrochemical performance as an anode material for lithium-ion batteries. *J. Mater. Chem. A* **2**, 3498–3504 (2014).
- Stephenson, T., Li, Z., Olsen, B. & Mitlin, D. Lithium ion battery applications of molybdenum disulfide (MoS<sub>2</sub>) nanocomposites. *Energy Environ. Sci.* **7**, 209–231 (2014).
- Xiao, J. *et al.* Exfoliated MoS<sub>2</sub> nanocomposite as an anode material for lithium ion batteries. *Chem. Mater.* **22**, 4522–4524 (2010).
- Wang, P. P., Sun, H. Y., Ji, Y. J., Li, W. H. & Wang, X. Three-dimensional assembly of single-layered MoS<sub>2</sub>. *Adv. Mater.* **26**, 964–969 (2014).
- Li, G. D. *et al.* Facile synthesis of hierarchical hollow MoS<sub>2</sub> nanotubes as anode materials for high-performance lithium-ion batteries. *CrystEngComm* **16**, 10754–10759 (2014).
- Zhang, L., Wu, H. B., Yan, Y., Wang, X. & Lou, X. W. Hierarchical MoS<sub>2</sub> microboxes constructed by nanosheets with enhanced electrochemical properties for lithium storage and water splitting. *Energy Environ. Sci.* **7**, 3302–3306 (2014).
- Yu, X. Y., Hu, H., Wang, Y. W., Chen, H. Y. & Lou, X. W. Ultrathin MoS<sub>2</sub> nanosheets supported on N-doped carbon nanoboxes with enhanced lithium storage and electrocatalytic properties. *Angew. Chem. Int. Ed.* **54**, 7395–7398 (2015).
- Ko, Y. N., Kang, Y. C. & Park, S. B. Superior Electrochemical properties of MoS<sub>2</sub> powders with a MoS<sub>2</sub>@void@MoS<sub>2</sub> configuration. *Nanoscale* **6**, 4508–4512 (2014).
- Ding, S., Zhang, D., Chen, J. S. & Lou, X. W. Facile synthesis of hierarchical MoS<sub>2</sub> microspheres composed of few-layered nanosheets and their lithium storage properties. *Nanoscale* **4**, 95–98 (2012).
- Wang, M., Li, G., Xu, H. Y. & Qian, Y. T., Yang, J. Enhanced lithium storage performances of hierarchical hollow MoS<sub>2</sub> nanoparticles assembled from nanosheets. *ACS Appl. Mater. Interfaces* **5**, 1003–1008 (2013).
- Wang, Z. *et al.* CTAB-assisted synthesis of single-layer MoS<sub>2</sub>-graphene composites as anode materials of li-ion batteries. *J. Mater. Chem. A* **1**, 2202–2210 (2013).
- Pham, V. H. *et al.* Liquid phase Co-exfoliated MoS<sub>2</sub> egraphene composites as anode materials for lithium ion batteries. *J. Power Sources* **244**, 280–286 (2013).
- Hou, Y. *et al.* N-doped graphene/porous g-C<sub>3</sub>N<sub>4</sub> nanosheets supported layered- MoS<sub>2</sub> hybrid as robust anode materials for lithium-ion batteries. *Nano Energy* **8**, 157–164 (2014).

21. Huang, G. C. *et al.* Graphene-like MoS<sub>2</sub>/graphene composites: cationic surfactant-assisted hydrothermal synthesis and electrochemical reversible storage of lithium. *Small* **9**, 3693–3703 (2013).
22. Cao, X. H. *et al.* Preparation of MoS<sub>2</sub>-coated three-dimensional graphene networks for high-performance anode material in lithium-ion batteries. *Small* **9**, 3433–3438 (2013).
23. Zhou, X. S., Wan, L. J. & Guo, Y. G. Synthesis of MoS<sub>2</sub> nanosheet–graphene nanosheet hybrid materials for stable lithium storage. *Chem. Commun.* **49**, 1838–1840 (2013).
24. Xiao, J. *et al.* Electrochemically induced high capacity displacement reaction of PEO/MoS<sub>2</sub>/graphene nanocomposites with lithium. *Adv. Funct. Mater.* **21**, 2840–2846 (2011).
25. Li, H. L. *et al.* MoS<sub>2</sub>/graphene hybrid nanoflowers with enhanced electrochemical performances as anode for lithium-ion batteries. *J. Phys. Chem. C* **119**, 7959–7968 (2015).
26. Wang, R. H. *et al.* Heat-induced formation of porous and free-standing MoS<sub>2</sub>/GS hybrid electrodes for binder-free and ultralong-life lithium ion batteries. *Nano Energy* **8**, 183–195 (2014).
27. Ma, L., Ye, J. B., Chen, W. X., Chen, D. Y. & Lee, J. Y. Gemini surfactant assisted hydrothermal synthesis of nanotile-like MoS<sub>2</sub>/graphene hybrid with enhanced lithium storage performance. *Nano Energy* **10**, 144–152 (2014).
28. Yu, H. L. *et al.* Three-dimensional hierarchical architectures constructed by graphene/MoS<sub>2</sub> nanoflake arrays and their rapid charging/discharging properties as lithium-ion battery anodes. *Chem. –Eur. J.* **19**, 5818–5823 (2013).
29. Teng, Y. Q. *et al.* MoS<sub>2</sub> Nanosheets vertically grown on graphene sheets for lithium-ion battery anodes. *ACS Nano* **10**, 8526–8535 (2016).
30. Zhu, C. B., Mu, X. K., Aken, P. A., Maier, J. & Yu, Y. Fast Li storage in MoS<sub>2</sub>-graphene-carbon nanotube nanocomposites: advantageous functional integration of 0D, 1D, and 2D nanostructures. *Adv. Energy Mater.* **5**, 1401170 (2015).
31. Wang, J. Z. *et al.* Development of MoS<sub>2</sub>-CNT composite thin film from layered MoS<sub>2</sub> for lithium batteries. *Adv. Energy Mater.* **3**, 798–805 (2013).
32. Kartick, B., Suneel Kumar, S. & Sourindra, M. MoS<sub>2</sub>-MWCNT hybrids as a superior anode in lithium-ion batteries. *Chem. Commun.* **49**, 1823–1825 (2013).
33. Zhang, L. & Lou, X. W. Hierarchical MoS<sub>2</sub> shells supported on carbon spheres for highly reversible lithium storage. *Chem. –Eur. J.* **20**, 5219–5223 (2014).
34. Yu, H. L. *et al.* Three-dimensional hierarchical MoS<sub>2</sub> nanoflake array/carbon cloth as high-performance flexible lithium-ion battery anodes. *J. Mater. Chem. A* **2**, 4551–4557 (2014).
35. Zhao, C. Y. *et al.* Thin MoS<sub>2</sub> nanoflakes encapsulated in carbon nanofibers as highperformance anodes for lithium-ion batteries. *ACS Appl. Mater. Interfaces* **6**, 6392–6398 (2014).
36. Xu, X. *et al.* A nanosheets-on-channel architecture constructed from MoS<sub>2</sub> and CMK-3 for high-capacity and long-cycle-life lithium storage. *Adv. Energy Mater.* **4**, 1400902 (2014).
37. Lupo, F. D. *et al.*  $\alpha$ -Fe<sub>2</sub>O<sub>3</sub> lithium battery anodes by nanocasting strategy from ordered 2D and 3D templates. *J. Alloys Compd.* **615**, S482–S486 (2014).
38. Cao, Z. Y. & Wei, B. Q.  $\alpha$ -Fe<sub>2</sub>O<sub>3</sub>/single-walled carbon nanotube hybridfilms as highperformance anodes for rechargeable lithium-ion batteries. *J. Power Sources* **241**, 330–340 (2013).
39. Wang, Y. G., Li, H. Q., He, P., Hosono, E. & Zhou, H. S. Nano active materials for lithium-ion batteries. *Nanoscale* **2**, 1294–1305 (2010).
40. Bruce, P. G., Scrosati, B. & Tarascon, J.-M. Nanomaterials for rechargeable lithium batteries. *Angew. Chem. Int. Ed.* **47**, 2930–2946 (2008).
41. Xie, J. F. *et al.* Controllable disorder engineering in oxygen-incorporated MoS<sub>2</sub> ultrathin nanosheets for efficient hydrogen evolution. *J. Am. Chem. Soc.* **135**, 17881–17888 (2013).
42. Yu, H. L. *et al.* A strategy to synergistically increase the number of active edge sites and the conductivity of MoS<sub>2</sub> nanosheets for hydrogen evolution. *Nanoscale* **7**, 8731–8738 (2015).
43. Baker, M. A., Gilmore, R., Lenardi, C. & Gissler, W. XPS Investigation of preferential sputtering of S from MoS and 2 determination of MoS stoichiometry from Mo and S peak x positions. *Appl. Surf. Sci.* **150**, 255–262 (1999).
44. Wang, H. W., Skeldon, P. & Thompson, G. E. XPS studies of MoS<sub>2</sub> formation from ammonium tetrathiomolybdate solutions. *Surf. Coat. Technol.* **91**, 200–207 (1997).
45. Lin, T. R., Wang, J., Guo, L. Q. & Fu, F. F. Fe<sub>3</sub>O<sub>4</sub>@ MoS<sub>2</sub> core-shell composites: preparation, characterization, and catalytic application. *J. Phys. Chem. C* **119**, 13658–13664 (2015).
46. Jiang, Y. Z. *et al.* Amorphous Fe<sub>2</sub>O<sub>3</sub> as a high-capacity, high-rate and long-life anode material for lithium ion batteries. *Nano Energy* **4**, 23–30 (2014).
47. Biesinger, M. C. *et al.* Resolving surface chemical states in XPS analysis of first row transition metals, oxides and hydroxides: Cr, Mn, Fe, Co and Ni. *Appl. Surf. Sci.* **257**, 2717–2730 (2011).
48. Xiong, Y. H. *et al.* Synthesis of magnetic porous g-Fe<sub>2</sub>O<sub>3</sub>/C@HKUST-1 composites for efficient removal of dyes and heavy metal ions from aqueous solution. *RSC Adv.* **5**, 5164–5172 (2015).
49. Fujii, T., De Groot, F. M. F. & Sawatzky, G. A. *In situ* XPS analysis of various iron oxide films grown by NO<sub>2</sub>-assisted molecular-beam epitaxy. *Phys. Rev. B* **59**, 3195–3202 (1999).
50. Sun, M., Dong, Y. Z., Zhang, G., Qu, J. H. & Li, J. H.  $\alpha$ -Fe<sub>2</sub>O<sub>3</sub> spherical nanocrystals supported on CNTs as efficient non-noble electrocatalyst for oxygen reduction reaction. *J. Mater. Chem. A* **2**, 13635–13640 (2014).
51. Pradhan, G. K., Padhi, D. K. & Parida, K. M. Fabrication of  $\alpha$ -Fe<sub>2</sub>O<sub>3</sub> nanorod/rGO composite: a novel hybrid photocatalyst for phenol degradation. *ACS Appl. Mater. Interfaces* **5**, 9101–9110 (2013).
52. Lu, Y. T. *et al.* MoS<sub>2</sub> nanoflowers consisting of nanosheets with a controllable interlayer distance as highperformance lithium ion battery anodes. *RSC Adv.* **5**, 7938–7943 (2015).
53. Fang, X. P. *et al.* Lithium storage in commercial MoS<sub>2</sub> in different potential ranges. *Electrochim. Acta* **81**, 155–160 (2012).
54. Hwang, H., Kim, H. & Cho, J. MoS<sub>2</sub> nanoplates consisting of disordered graphene-like layers for high rate lithium battery anode materials. *Nano Lett.* **11**, 4826–4830 (2011).
55. Chang, K. & Chen, W. X. L-cysteine-assisted synthesis of layered MoS<sub>2</sub>/graphene composites with excellent electrochemical performances for lithium ion batteries. *ACS Nano* **5**, 4720–4728 (2011).
56. Ye, J., Zhang, J., Wang, F. X., Su, Q. M. & Du, G. H. One-pot synthesis of Fe<sub>2</sub>O<sub>3</sub>/graphene and its lithium-storage performance. *Electrochim. Acta* **113**, 212–217 (2013).
57. Liu, J. L. *et al.* Three dimensionals  $\alpha$ -Fe<sub>2</sub>O<sub>3</sub>/polypyrrole (ppy) nanoarray as anode for micro lithium ion batteries. *Nano Energy* **2**, 726–732 (2013).
58. Zhou, G. W. *et al.* Facile spray drying route for the three-dimensional graphene encapsulated Fe<sub>2</sub>O<sub>3</sub> nanoparticles for lithium ion battery anodes. *Ind. Eng. Chem. Res.* **52**, 1197–1204 (2013).
59. Xu, S. M. *et al.*  $\alpha$ -Fe<sub>2</sub>O<sub>3</sub> multi-shelled hollow microspheres for lithium ion battery anodes with superior capacity and charge retention. *Energy Environ. Sci.* **7**, 632–637 (2014).
60. Gao, G. X., Yu, L., Wu, H. B. & Lou, X. W. Hierarchical tubular structures constructed by carboncoated  $\alpha$ -Fe<sub>2</sub>O<sub>3</sub> nanorods for highly reversible lithium storage. *Small* **9**, 1741–1745 (2013).
61. Zhu, X. D. *et al.* Creating a synergistic interplay between tubular MoS<sub>2</sub> and particulate Fe<sub>3</sub>O<sub>4</sub> for improved lithium storage. *Chem. Commun.* **51**, 11888–11891 (2015).

62. Chen, Y., Song, B. H., Tang, X. H., Lu, L. & Xue, J. M. Ultrasmall Fe<sub>3</sub>O<sub>4</sub> nanoparticle/MoS<sub>2</sub> nanosheet composites with superior performances for lithium ion batteries. *Small* **10**, 1536–1543 (2014).
63. Pan, L., Zhu, X. D., Xie, X. M. & Liu, Y. T. Delicate ternary heterostructures achieved by hierarchical Co-assembly of Ag and Fe<sub>3</sub>O<sub>4</sub> nanoparticles on MoS<sub>2</sub> nanosheets: morphological and compositional synergy in reversible lithium storage. *J. Mater. Chem. A* **3**, 2726–2733 (2015).
64. Wan, Z. M. *et al.* Core–shell structure of hierarchical quasi-hollow MoS<sub>2</sub> microspheres encapsulated porous carbon as stable anode for li-ion batteries. *Small* **10**, 4975–4981 (2014).
65. Lu, L. *et al.* Monolithic Fe<sub>2</sub>O<sub>3</sub>/graphene hybrid for highly efficient lithium storage and arsenic removal. *Carbon* **67**, 500–507 (2014).
66. Zhang, L., Wu, H. B., Madhavi, S., Hng, H. H. & Lou, X. W. Formation of Fe<sub>2</sub>O<sub>3</sub> microboxes with hierarchical shell structures from metal–organic frameworks and their lithium storage properties. *J. Am. Chem. Soc.* **134**, 17388–17391 (2012).
67. Pan, L., Liu, Y. T., Xie, X. M. & Zhu, X. D. Coordination-driven hierarchical assembly of silver nanoparticles on MoS<sub>2</sub> nanosheets for improved lithium storage. *Chem. Asian J.* **9**, 1519–1524 (2014).
68. Xu, X., Fan, Z. Y., Ding, S. J., Yu, D. M. & Du, Y. P. Fabrication of MoS<sub>2</sub> nanosheet@TiO<sub>2</sub> nanotube hybrid nanostructures for lithium storage. *Nanoscale* **6**, 5245–5250 (2014).
69. Park, S. K. *et al.* A simple l-cysteine-assisted method for the growth of MoS<sub>2</sub> nanosheets on carbon nanotubes for high-performance lithium ion batteries. *Dalton Trans.* **42**, 2399–2405 (2013).
70. Han, S. *et al.* Ternary MoS<sub>2</sub>/SiO<sub>2</sub>/graphene hybrids for high-performance lithium storage. *Carbon* **81**, 203–209 (2015).
71. Liu, H. *et al.* Porous tremella-like MoS<sub>2</sub>/polyaniline hybrid composite with enhanced performance for lithium-ion battery anodes. *Electrochim. Acta* **167**, 132–138 (2015).
72. Yu, X. B. *et al.* Growth of hollow transition metal (Fe, Co, Ni) oxide nanoparticles on graphene sheets through kirkendall effect as anodes for high-performance lithium-ion batteries. *Chem. –Eur. J.* **22**, 1638–1645 (2016).
73. Poizot, P., Laruelle, S., Grugeon, S., Dupont, L. & Tarascon, J.-M. ChemInform abstract: nano-sized transition-metal oxides as negative-electrode materials for lithium-ion batteries. *Nature* **407**, 496–499 (2000).
74. Hassan, M. F., Guo, Z. P., Chen, Z. & Liu, H. K. Carbon-coated MoO<sub>3</sub> nanobelts as anode materials for lithium-ion batteries. *J. Power Sources* **195**, 2372–2376 (2010).

## Acknowledgements

This work is supported by the National Natural Science Foundation of China (Grant no. 51572051), the Natural Science Foundation of Heilongjiang Province (E2016023), the 111 project (B13015) of the Ministry of Education of China to the Harbin Engineering University, and also the Open Project Program of Key Laboratory for Photonic and Electric Bandgap Materials, Ministry of Education, Harbin Normal University, China.

## Author Contributions

Y.C. and C.L. proposed the research direction and guided the project. B.Q. designed and performed the experiments. Y.C., B.Q. and C.L. analysed and discussed the experimental results and drafted the manuscript. X.Z. carried out TEM measurements. L.L., Y.S. and C.Y. carried out some supporting experiments. All authors have read and approved the final manuscript.

## Additional Information

**Supplementary information** accompanies this paper at <http://www.nature.com/srep>

**Competing financial interests:** The authors declare no competing financial interests.

**How to cite this article:** Qu, B. *et al.* Ultrasmall Fe<sub>2</sub>O<sub>3</sub> nanoparticles/MoS<sub>2</sub> nanosheets composite as high-performance anode material for lithium ion batteries. *Sci. Rep.* **7**, 42772; doi: 10.1038/srep42772 (2017).

**Publisher's note:** Springer Nature remains neutral with regard to jurisdictional claims in published maps and institutional affiliations.



This work is licensed under a Creative Commons Attribution 4.0 International License. The images or other third party material in this article are included in the article's Creative Commons license, unless indicated otherwise in the credit line; if the material is not included under the Creative Commons license, users will need to obtain permission from the license holder to reproduce the material. To view a copy of this license, visit <http://creativecommons.org/licenses/by/4.0/>

© The Author(s) 2017